Full Length Article

Quantification of hydrogen in nanostructured hydrogenated passivating contacts for silicon photovoltaics combining SIMS-APT-TEM: A multiscale correlative approach

Soupitak Pal [a],[*], Jenifer Barrirero [b], Mario Lehmann [c], Quentin Jeangros [c], Nathalie Valle [d], Franz-Josef Haug [c], Aïcha Hessler-Wyser [c], C.N. Shyam Kumar [a], Frank Mücklich [b], Tom Wirtz [a], Santhana Eswara [a],[*]

[a] Advanced Instrumentation for Nano-Analytics (AINA), Luxembourg Institute of Science and Technology (LIST), Materials Research and Technology Department, 41, Rue Du Brill, L-4422 Belvaux, Luxembourg
[b] Functional Materials, Department of Materials Science, Saarland University, D-66123 Saarbrücken, Germany
[c] Ecole Polytechnique Fédérale de Lausanne (EPFL), Institute of Microengineering (IMT), Photovoltaics and Thin Film Electronics Laboratory, Rue de La Maladière 71b, 2002 Neuchâtel, Switzerland
[d] Advanced Characterization Platform (ACP), Luxembourg Institute of Science and Technology (LIST), Materials Research and Technology Department, 41, Rue Du Brill, L-4422 Belvaux, Luxembourg

ARTICLE INFO

ABSTRACT

Multiscale characterization of the hydrogenation process of silicon solar cell contacts based on c-Si/SiO$_x$/nc-SiC$_x$(p) has been performed by combining dynamic secondary ion mass-spectrometry (D-SIMS), atom probe tomography (APT), and transmission electron microscopy (TEM). These contacts are formed by high-temperature firing, which triggers the crystallization of SiC$_x$, followed by a hydrogenation process to passivate remaining interfacial defects. Due to the difficulty of characterizing hydrogen at the nm-scale, the exact hydrogenation mechanisms have remained elusive. Using a correlative TEM-SIMS-APT analysis, we are able to locate hydrogen trap sites and quantify the hydrogen content. Deuterium (D), a heavier isotope of hydrogen, is used to distinguish hydrogen introduced during hydrogenation from its background signal. D-SIMS is used, due to its high sensitivity, to get an accurate deuterium-to-hydrogen ratio, which is then used to correct deuterium profiles extracted from APT reconstructions. This new methodology to quantify the concentration of trapped hydrogen in nm-scale structures sheds new insights on hydrogen distribution in technologically important photovoltaic materials.

1. Introduction

The world has seen a tremendous improvement in semiconductor device technology, thanks to miniaturization of devices along with the drastic improvements in thin-film deposition technologies. Deposition of both nano and sub-nanometer thickness is readily achievable with high precision. Hence, a marked improvement has clearly been seen in the performances of the devices. A similar trend has been seen in photovoltaics, where solar cell efficiency has been continuously increasing [1,2]. This high efficiency is typically achieved by minimizing recombination losses at the electrical contact through the deposition of a thin layer of material, which reduces the defect density responsible for recombination losses [3,4]. Over the past years, the so-called poly-Si

passivating contacts have attracted attention, as they display excellent conversion efficiencies (up to 26.1% in research and 24.9% in industry [5–8]), while being compatible with the high temperature processes (>800 °C) commonly used in industry, as for example the firing through metallization process [9,10]. These contacts typically consist of a thin (≈1.2–3.6 nm) layer of SiO$_x$ grown on the wafer's surface and capped with a highly doped poly-Si layer. In most cases, a subsequent hydrogenation step is necessary, during which hydrogen diffuses towards the wafer-SiO$_x$ interface where it gets trapped and passivates defects (dangling bonds), thus reducing the recombination losses [11–14]. Direct quantification of H within the layer and at the interface is still missing. Thus, to precisely control the device's electrical characteristics, three-dimensional characterization of the distribution of H and mapping
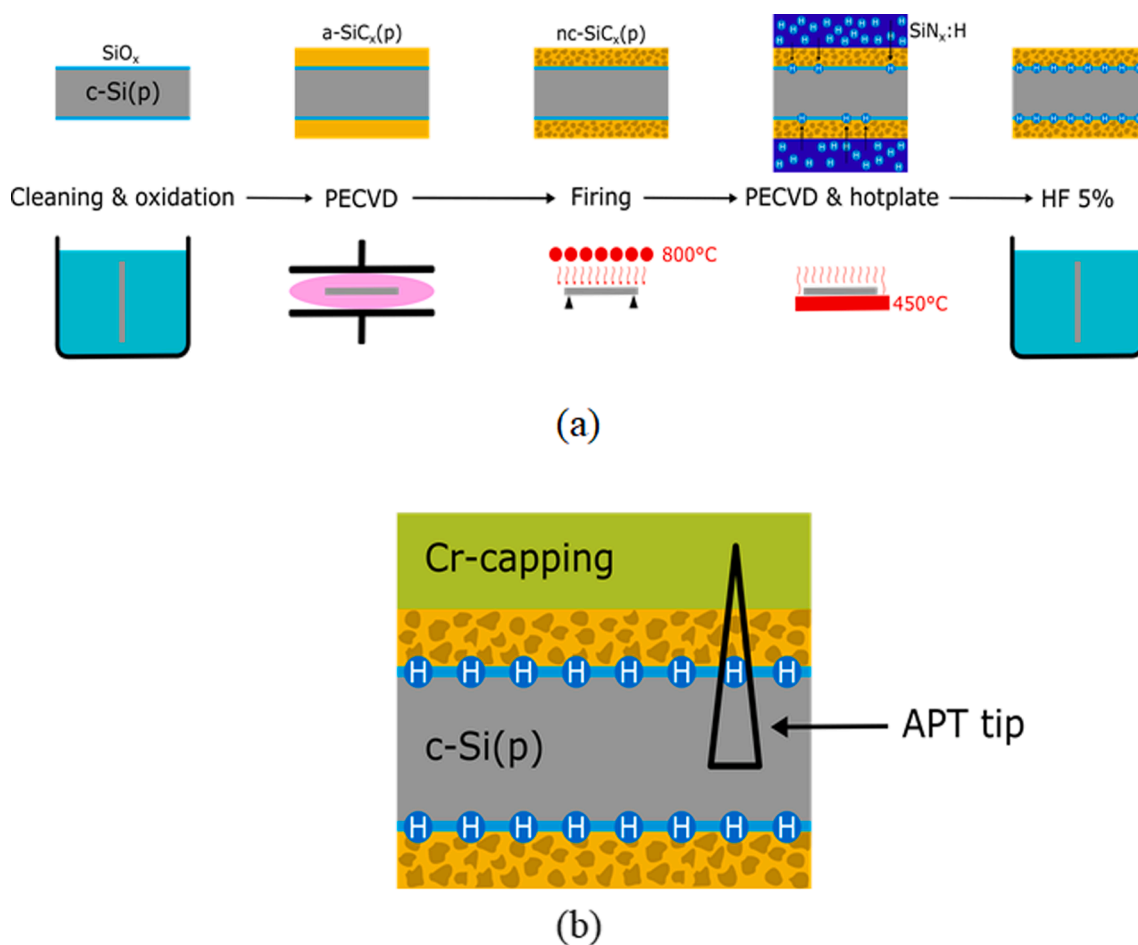
Fig. 1. (a) Schematics of fabrication steps of fired passivation contact; b) schematic of the location, from where the APT tip is extracted.

of its trapping sites with a subnanometer spatial resolution and its quantification is critically important.

Simultaneous detection, mapping, and quantification of hydrogen at a length scale less than 5 nm is a daunting task and cannot be tackled with a single technique. Thermal desorption spectroscopy is able to detect H but fails in mapping complex structures [15]. Secondary ion mass spectrometry (SIMS) possesses excellent mass-resolution capability with high sensitivity. SIMS is one of the techniques that has been successfully employed in distinguishing H and D contributions in an analyzed sample. However, it may lack spatial resolution for ultrathin layers [11,14,16]. Transmission electron microscopy (TEM) allows mapping of H atoms only in rare cases like graphene [17]. Recently, atom probe tomography has been gaining attention due to its capability to, e.g., 3D mapping of hydrogen at precipitates and grain boundaries in steel [18–22]. The implementation of a pulsed laser has extended the technique's applicability to semiconductor materials and devices [23–25]. However, the observation and quantitative analysis of H remains difficult since a significant amount of the detected H comes from the residual gas in the analysis chamber during the APT measurement [26–28]. Therefore, much effort has been devoted to introducing deuterium (D), an isotope of H, to study the relationship between mechanical properties and distribution of H species [29–31]. The charged D can quickly diffuse out of the specimen unless kept under cryogenic conditions before the APT measurement [21]. However, Takamizawa et al. introduced D into Si by ion implantation and demonstrated that D partly became trapped in the defects induced by ion implantation and partly bonded with Si with D remaining in the sample, even at room temperature [32]. On the other hand, SIMS has the capability to differentiate H and D, while keeping a high-sensitivity with a mass

resolution (m/Δm) ranging from ≈300–10,000. However, quantification of SIMS intensities is not straightforward because of strong variations in the ionization yields depending on the matrix (i.e., matrix effect) [33]. A standard reference sample is always required in order to quantify the obtained data [16]. The combination of information from both APT and SIMS to get a 3D elemental distribution have already been used to characterize dopant contribution in a nanostructured semiconductor device, deuterium in zirconium oxide or boundary segregation in high-strength steel [34–37].

Here, we propose a new correlative methodology to accurately quantify the H and D concentration after hydrogenation of a so-called Fired Passivating Contact [38], one type of high temperature passivating contact used in solar cells layers mentioned earlier, using a multiscale characterization approach. SIMS is employed to obtain depth profiles of the elements present within the contact, including the H and D profiles. In addition to SIMS, APT is used to reveal the 3D distribution of elements within the contact. APT data is further corroborated using high-resolution scanning transmission electron microscopy (STEM). These techniques are then combined to characterize the microstructure along with its chemical constituents. The ≈1.5 nm-thin non-stoichiometric SiO_x is identified to trap both H and D. The novelty of the current work lies in the quantification of the H and D with nanometer spatial resolution within the thin layer. Our novel correlative methodology extracts the composition from APT using SIMS data as input. More specifically, the background contribution from the residual chamber gas present in both the APT and SIMS data during H and D analysis is deconvoluted to quantify both H and D present within the layers. Investigations relying only on SIMS or APT to quantify hydrogen/deuterium require a vast number of control experiments to determine
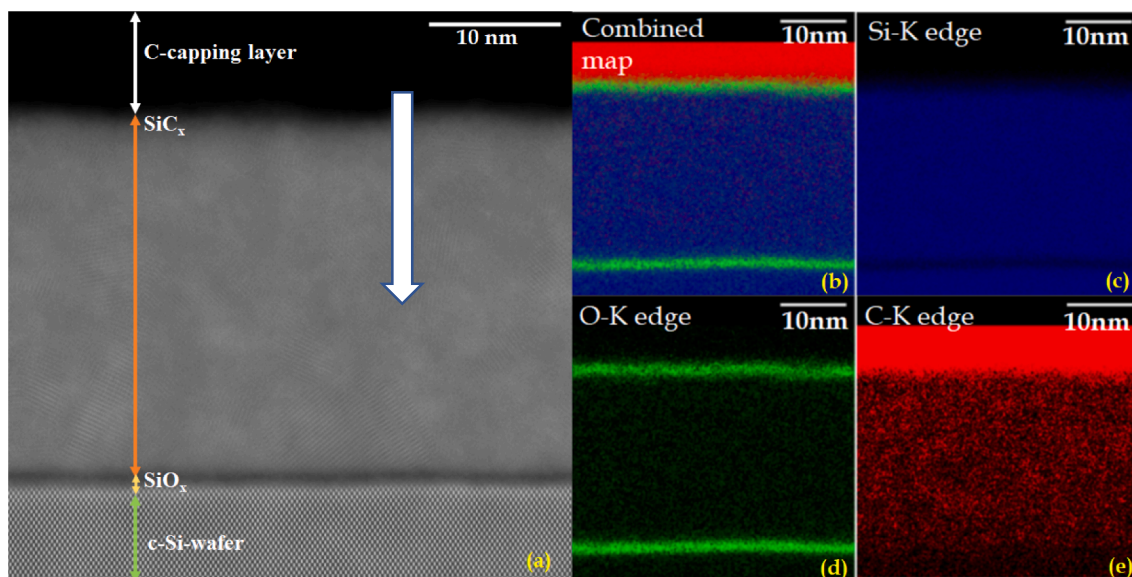
Fig. 2. (a) High-resolution HAADF-STEM image of the cross-section of the fired contact, (b) combined elemental distribution map measured using EDS, (c), (d) and (e) are the individual elemental maps of Si-K edge, O-K edge and C-K edge, respectively. The larger white arrow indicates the direction of hydrogen diffusion.

the background contribution [13,39–43]. The new correlative analysis methodology that is proposed here simplifies the procedure to quantify H and D.

2. Materials and methods

Details of the solar-cell fabrication were given elsewhere [38]. Here, we briefly describe the sample fabrication steps. Symmetrical solar-cell test structures were deposited on a double-side polished p-type float zone (1 0 0) wafer that was 280 μm-thick and exhibited a resistivity of 3 Ωcm. After a wet chemical cleaning, a ~1.3 nm SiO_x layer was grown on the wafer surface by exposing the wafer to UV radiation in ambient air (2 min each side) [44–46]. On top of the SiO_x layer, we deposited by Plasma Enhanced Chemical Vapour Deposition (PECVD) at 200 °C a ~30 nm-thick (as-deposited thickness) hydrogenated amorphous silicon layer featuring some carbon (a-SiC_x(p-type): H) (~7 at.% of carbon) [38]. Subsequently, the samples were fired at ~800 °C for 3 s. During this step, the initially amorphous film (a-SiC_x(p): H) crystallized into nanocrystalline nc-SiC_x(p), and hydrogen effused from that layer. Re-hydrogenation was then performed via hydrogen diffusion from a ~70 nm thick sacrificial layer of SiN_x:H. The latter was deposited at 250 °C in an in-house built PECVD tool and optimized for the release of H during a 30 min hotplate annealing at 450 °C [47]. After this hydrogenation step, the SiN_x:H layer was removed in an HF solution. A representative schematic figure illustrating the fabrication sequences is shown in Fig. 1a for better clarity.

Deuterium (D_2) was diffused into the layer alongside hydrogen (H_2) to ease the SIMS analysis and help in the identification of hydrogen trap sites. To include deuterium in the layers, the H_2 gas flow was replaced by D_2 during the SiC_x(p): H/D and SiN_x:H/D PECVD processes. Note that during these PECVD depositions, SiH_4 and NH_3 or trimethyl borane gas flows were present alongside D_2. Thus, both deuterium and hydrogen were incorporated in these layers and diffused alongside each other during the hydrogenation step. Due to its higher mass, Deuterium has a lower diffusivity than hydrogen [48]. Thus, the kinetics of the hydrogenation process are expected to be slightly different. However, the passivation mechanism should be identical, as the nature of bonding for the two isotopes with Si is the same.

A multi-scale characterization of the H and D present in the samples was performed using D-SIMS, APT and TEM. The D-SIMS depth profiles were obtained using a CAMECA SC-Ultra instrument with Cs^+ primary ions with a 1 keV impact energy to balance resolution and sensitivity in the MCs_2^+ mode used. A low-energy primary ion beam helps reaching an equilibrium sputtering and ionization conditions on pristine surfaces rapidly. The primary ion current was set to 2.39 nA. The ion beam was scanned over an area of 300 μm × 300 μm, and the signal was acquired from an inner area of 62 μm in diameter. The acceptance energy window was 19 eV. Deuterium was analyzed in the MCs_2^+ mode as DCs_2^+. The ion yield for $H_2Cs_2^+$ is negligible in comparison to DCs_2^+ which is also confirmed by the fact that the SIMS D/H ratio (Fig. 8a) reaches the natural abundance ratio in the silicon substrate. Hence, a high mass resolution was not needed and a value of 400 was selected to optimize sensitivity. Ions were collected from an area of 62 μm in diameter, with a depth resolution of ~a few nm (not element dependent). The instrument was operated with a field aperture of 750 μm, contrast aperture of 300 μm, entrance and exit slit of 400 and 600 μm, respectively. The SIMS sputtering time was converted into depth, assuming a linear erosion after measuring the crater depth at the end of the experiment using a KLA-Tencor P17 profilometer. The microstructure of the contact was assessed after firing and re-hydrogenation using TEM. For that purpose, a cross-section were extracted using the conventional focused ion beam (FIB) lift-out method, which was performed in a Zeiss NVision 40 FIB/scanning electron microscope (SEM) using a final Ga^+ voltage of 2 kV. In an image and probe Cs-corrected TFS Titan Themis microscope, STEM-high angle annular dark field (HAADF) micrographs were acquired combined with energy dispersive X-ray (EDX) spectroscopy maps using a beam current of 400 pA at 200 kV. EDX spectra were quantified using algorithms implemented in the TFS Velox software (multi-polynomial background model with 0-order in the fitted regions, no correction for absorption, Brown-Powell ionization cross-section model). Fourier and inverse Fourier transforms of high-resolution STEM-HAADF images were computed using the software Digital Micrograph (Gatan).

The quantification of H and D at the atomic length scale was performed using a local electrode atom probe LEAP 3000X HR (CAMECA, USA) at a sample temperature of about 60 K, a pulse frequency of 100 kHz, laser energy between 0.7 and 1 nJ, a rate of evaporation of 1 count per 200 pulses with a base pressure of 5×10^{-11} Torr in the analysis chamber. The atomic detection efficiency of the instrument is 37%. Successful runs were manually stopped after 5 million atoms to measure across all layers of interest and substrate. The percentage of single hits on the detector during the acquisition was above 90%. Datasets were reconstructed and analyzed by the commercial CAMECA Integrated
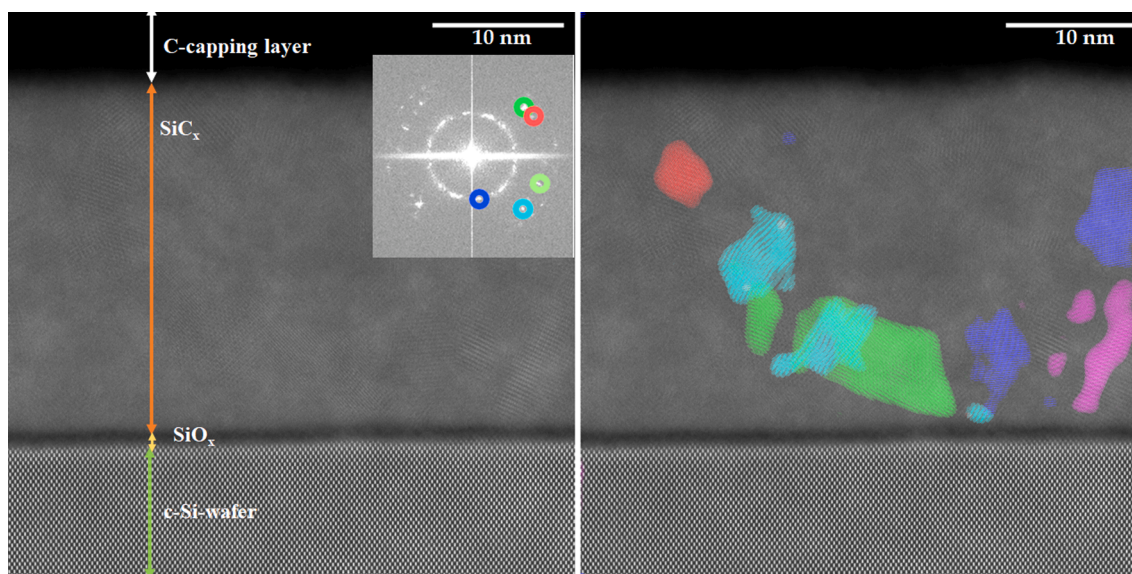
Fig. 3. (a) HRSTEM image of the fired contact, inset showing the FFT pattern captured from the SiC_x layer; (b) showing the marked nanoclusters corresponding to the marked spots from the FFT pattern and superimposed on the HRSTEM image. Individual color code shows the cluster associated with the corresponding colored spot in the inset FFT pattern in (a).

Visualization and Analysis Software (IVAS 3.6.8) package. A typical mass-spectrum is shown in SI Fig. S1, where the individual peaks are identified based on their mass to charge ratios.

APT specimens from the fired sample were prepared in a FIB/SEM Helios Nanolab 600 (TFS) by the lift-out method described in [49]. Fig. 1b displays the location from where the APT tips are extracted with the help of a schematic. A 150 nm-thick Cr-capping layer was deposited on top of the solar-cell sample by a low-energy, low-temperature physical vapor deposition to enable the APT analysis of the contact stack with a field-of-view of about 1600 nm^2. The use of the Cr-capping layer and a final low energy milling at 2 kV protected the surface from Ga^+-beam induced damage.

3. Results and discussion

Fig. 2 displays a cross-sectional STEM HAADF image along with the EDX elemental distribution maps (Si, O and C). The STEM image and the EDX map highlight the SiO_x layer, sandwiched in between the Si and SiC_x layers, has an average uniform thickness of 1.4 ± 0.2 nm, deduced from the TEM images using Image-J software from 10 different measurements across the whole image. SiC_x layer has an average thickness of 27 ± 0.3 nm after firing. The C content on top of the contact stack, see Fig. 2b, is due to the protective capping C-layer deposited during FIB sample preparation to prevent damage from the Ga^+-beam. A native oxide layer formed on top of the SiC_x layer during processing, as seen in Fig. 2. High-resolution STEM images are shown in Fig. 3. Inverse Fourier transforms (IFFT) of a selection of Si reflections reveal that the SiC_x layer partially crystallized during firing and now exhibits crystals with a size ranging from $\approx$5–10 nm. STEM micrographs and corresponding EDX line profiles of both the as-deposited and fired contact stacks are shown in SI. Fig. 2. The thickness of the as-deposited SiC_x layer measured from the STEM image is ~32 nm, compared to ~25 nm after firing. The ~15% shrinkage in the thickness of the SiC_x layer results from its crystallisation and a loss of volatile species such as hydrogen.

SIMS depth profiling reveals some of the intricate compositional details regarding the layer structure, as seen in Fig. 4. As discussed in Section 3.1, the thickness of the oxide layer is too thin to be measured accurately by SIMS (appears as ~5 nm-thick instead of 1.3 nm-thin). Peaks in both the O and H profiles coincide, indicating a trapping of H in the oxide layer. A peak in the D signal is also observed in the oxide layer.

However, the D signal peak does not coincide with the H and O peaks. A difference of ~2 nm in depth is observed between the D and H peaks (Fig. 4b). Interestingly, a high degree of fluctuation in the C, B, Si, and signals is also observed in the SiC_x layer. Neither C nor B are detected within the oxide layer.

APT was then used to investigate in greater details the structure and chemistry of the contact (Figs. 5–7). The identification of the different elements was performed using the APT mass-spectrum, see SI. Fig. S1. The APT analysis finds an oxide layer thickness of ~1.5 nm (Fig. 5a and b), in line with the TEM data. Fig. 5c displays the concentration profile across the reconstruction, whereas a magnified version of the profile at the oxide layer is shown in the inset. Si, O, C, and B are detected within the oxide layer. C and B rich clusters can be identified in the SiC_x layer as shown in the *iso*-concentration surfaces and 2D-contour plots shown in Fig. 6e–g. Some heterogeneity in the C distribution was also identified by EDX (Fig. 2a). The clusters seen by APT have roughly the same size as the Si crystals visualized by STEM imaging. The APT concentration profile of C in Fig. 5c shows oscillations within the SiC_x layer which can be attributed to C rich nanoclusters.

By APT, the Si to O ratio within the oxide layer is nearly 75:25, whereas the percentage of C and B within the oxide layer are ~6.6 at.% and ~3 at.%, respectively. Overall, the APT results indicate that the oxide layer is non-stoichiometric, confirming previous reports [46,50]. The peak at 1 Da (Dalton) in the APT mass-spectra gives a clear indication of the presence of H in the analysed structure. However, the peak at 2 Da cannot be unambiguously assigned to D due to presence of molecular H_2^+ ions (see Fig. 7). We will therefore label this peak 2 Da and will not assign it to a specific atom. In line with the SIMS results (Fig. 4), both 1 Da/H and 2 Da are detected in the oxide layer, highlighting the effectiveness of H and D to passivate interfacial defects (Fig. 5c) [14]. The ratio of the H to 2 Da peaks within the oxide layer is $\approx$ 4:1. To quantify the hydrogen and deuterium distribution, we will now combine techniques, as discussed in the next paragraphs.

3.1. Effect of chamber gas on SIMS profile, peak-shift, and blurring in SIMS

Effect of chamber gas, especially hydrogen, is unavoidable even when operating the instrument at a high vacuum of 10^{-8} Torr (1.33×10^{-8} mbar). During D-SIMS analysis, secondary ions are emitted from
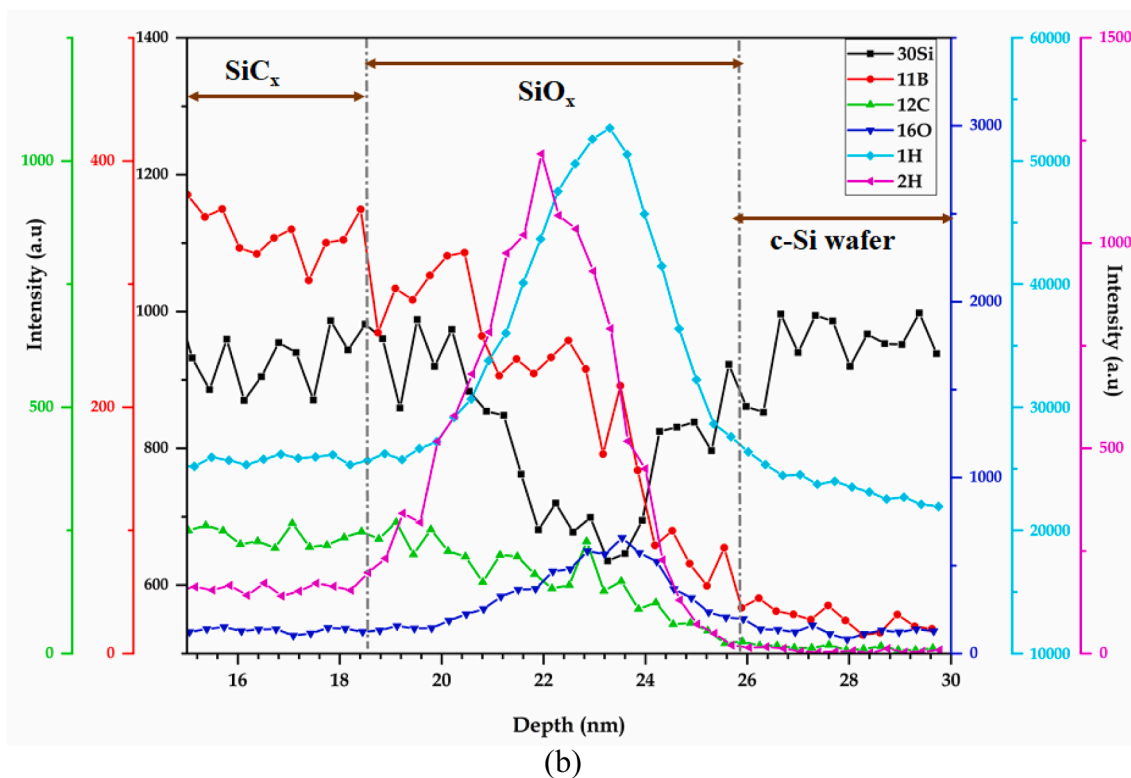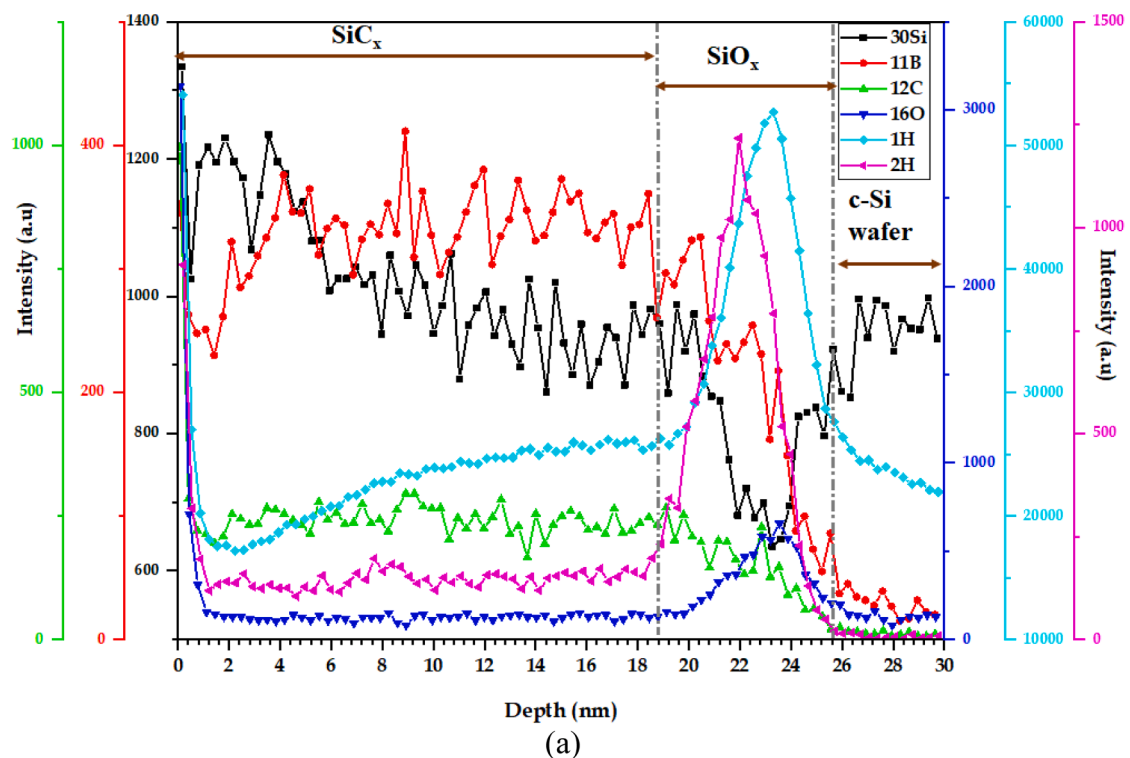
(a)

(b)

Fig. 4. (a) SIMS depth profile showing different elements; (b) magnified portion from Fig. a, showing the oxide layer.

the top one or two monolayers of the sample surface, which is always under constant bombardment of residual gas species (H_2, H_2O, and hydrocarbon). Some of them stick to the sample surface, and, during the analysis, they cannot be differentiated from the actual hydrogen content within the sample [51,52]. Therefore, true H concentration within an analyzed sample always suffers from a noticeable amount of "instrumental background" contribution derived from chamber gas. The magnitude of the background depends on factors like a) arrival rate of

atoms from the gas phase, b) sticking coefficient of the arrival gas atoms, c) removal rate of the sample during sputtering [52]. It has been previously reported that background contribution in SIMS data is more or less constant after an initial transient period [40,52–54]. After carefully analyzing the hydrogen profile, see SI. Fig. 3f, it becomes evident that after an initial transient period, the H signal intensity continuously rises in the SiC_x layer. It reaches a peak in the oxide layer, and finally, it starts to decrease when reaching the c-Si wafer. The concomitant increase of H
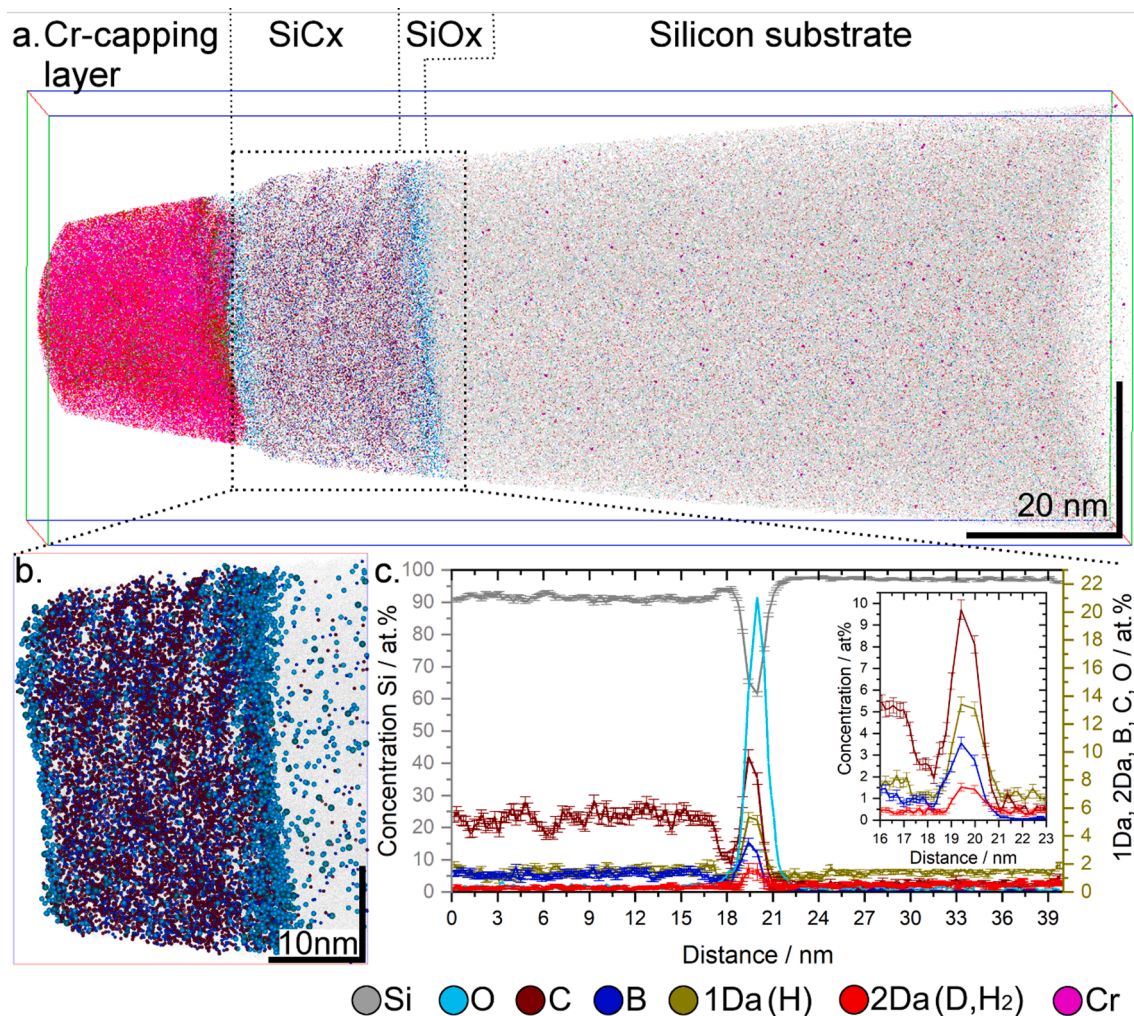
Fig.5. (a) 3D atom map of the analysed volume; (b) inset of (a) showing the oxide layer (atoms represented as spheres); (c) Concentration profile across the SiC_x, SiO_x and Si substrate. An inset of the SiO_x layer highlights the accumulation of H and D at this layer.

signal in the SiC_x layer, followed by a peak in the SiO_x layer, indicates trapping of hydrogen in those layers. Since it is already established that background H signal contribution in SIMS should be constant after an initial transient period. The SIMS D signal is higher in the SiC_x layer than the wafer side, followed by a peak at the SiO_x layer. Moreover, the SIMS D/H ratio at the substrate side reaches the natural abundance of D (see Fig. 8a) and indicates the absence of diffused hydrogen in the wafer side. The detected H and D in the wafer side originates from the chamber gas, explaining why the D/H ratio in SIMS reaches the natural abundance in the wafer. It is also expected that the D distribution and its trapping within the layers will be qualitatively same as H, as the chemical affinity of both species is similar. The only difference is their mass, which is one of the prime motivations for us to diffuse D along with H to locate possible trap sides for H within the layers without any interference from the adsorbed chamber gases. The full width at half maximam (FWHM) values for both 1H and D peak, located within the SiO_x layer, observed in the SIMS depth profile of Fig. 4 are 2.95 ± 0.1 and 3.05 ± 0.2 nm, respectively. They are not that different in their magnitude; however, both the peaks do not coincide. The peak in O signal and cusp in Si signal in the SiO_x layer coincide well with the 1H signal but not with the 2H or D signal, see Fig. 4. On the other hand, both C and B do not exhibit any peak at all in the SiO_x layer. Interestingly, the APT composition profile of Fig. 5c shows that within the SiO_x layer, O, C, B, H, and 2 Da peaks and Si cusp coincide with each other. In order to explain a shift in the 1H and 2D peak in SIMS and disappearance of the B,

C peaks in the SiO_x layer, let's understand SIMS signal production from the perspective of secondary ion productions and recorded intensity in the detector. Excellent sensitivity coupled with very high precision for SIMS is due to its ability to perform analysis in such a way that the ionized fraction of the secondary particles is high (sometimes even greater than 1%) and, absence of an inherent instrumental background [55]. In order to achieve this, a mono-energy primary ion beam 0.2–15 keV hits the sample surface to sputter out material. Interaction of the primary beam with sample surface deposits a large amount of energy and knocks off atoms from their lattice sites by producing collision cascades. The surface composition is typically modified with reactive ions species to produce favorable ion yields. While after attaining a stationary concentration of the primary ions, it increases the matrix's ions yield [55]. Therefore, due to the collision cascade, chaotic relocation of matrix atoms starts to occur through ion beam mixing [56]. The net effect yields mass transport and distortion of the actual profile of impurity elements, as well as a shift in the distribution of the profile of the impurity element within a thin layer. This effect can be understood with the help of the schematic shown in SI. Fig. S4. For a perfect experiment, the intensity count Y_{xi} from a thin layer impurity of concentration C_{xi} within a matrix at a depth $i\Delta z$ from the surface can be written in the form of

$$Y_x(\emptyset) = R_x C_x(z) + n \tag{1}$$

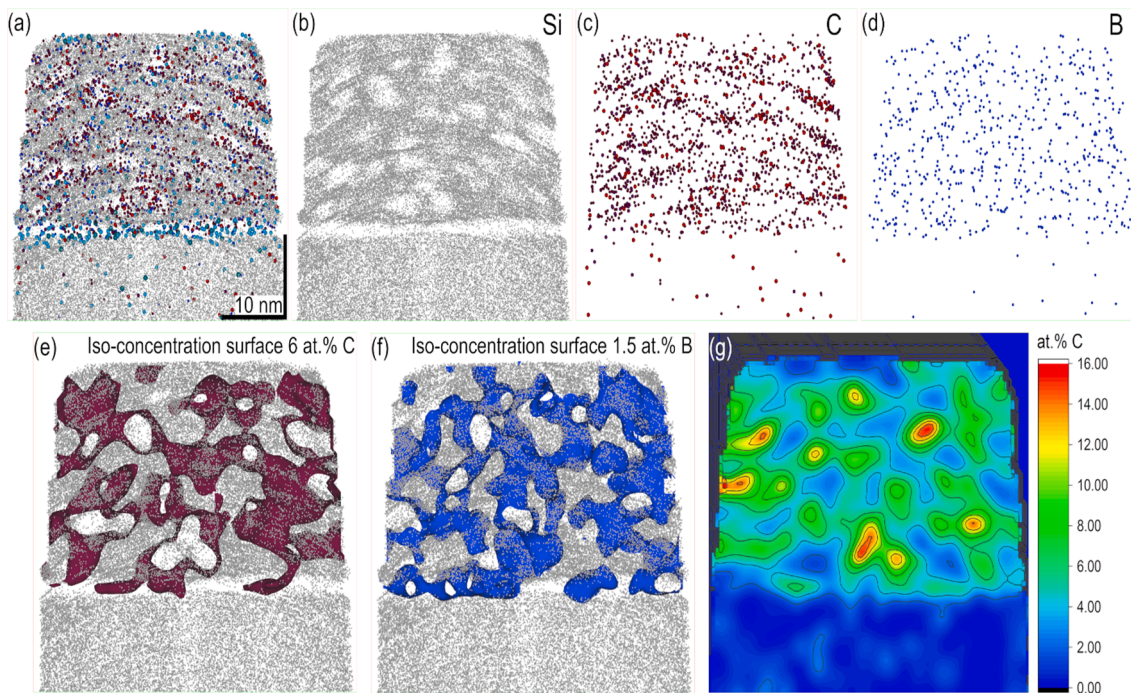The Δz is the incremental depth, $\Delta\emptyset$ is the incremental dose of the

Fig. 6. (a) Reconstructed SiC$_x$ layer, (b) Si, (c) C, (d) B maps; e) 6 at.% C *iso*-concentration surface; (f) 1.5 at.% B *iso*-concentration surface (g) 2D-concentration plots of C, colour ranges from 0 to 15 at.%. All images in Fig. 6 are taken from a 3 nm thick slice through the reconstruction.
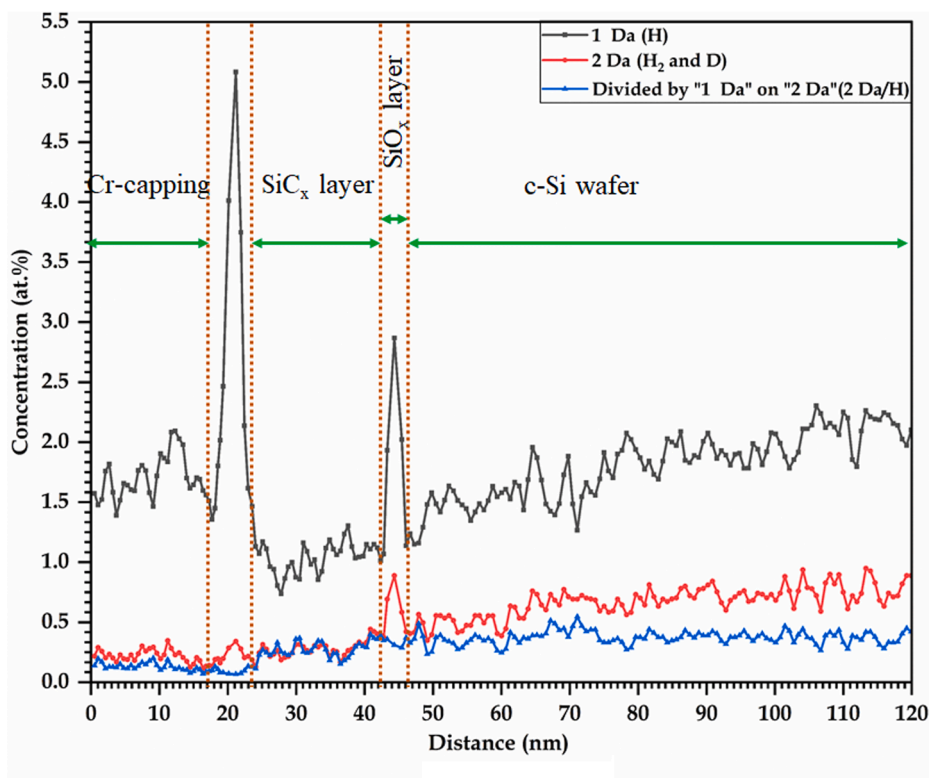

Fig. 7. 1 Da (H), 2 Da (H$_2$ and D) and 2 Da/H ratio profile from APT for the whole reconstructed tip is shown, individual layers are appropriately labelled.

primary ion beam, R_x is the nonlinear response function of the matrix, whereas n is the additive instrumental noise. In real experiments, the secondary ion contributions do not only come from the ith ordinate or location; Y$_{xi}$ contains contribution from layers C$_{i-j}$…C$_i$…Ci$_{+k}$, because of local redistribution of impurity atoms due to ion-beam mixing [57]. Therefore Eq. (1), can be rewritten for the real experiments as

$$Y_x(\varnothing) = n + \int d\varnothing^{'} R_x(\varnothing, \varnothing^{'}) Y_{x(perfect)}(\varnothing^{'}) \qquad (2)$$

where R$_x$(ø,ø′) is the response function varies with both ø and z [57]. Eq. (2) justifies why we have seen a broadening H, D and O peaks at the SiO$_x$
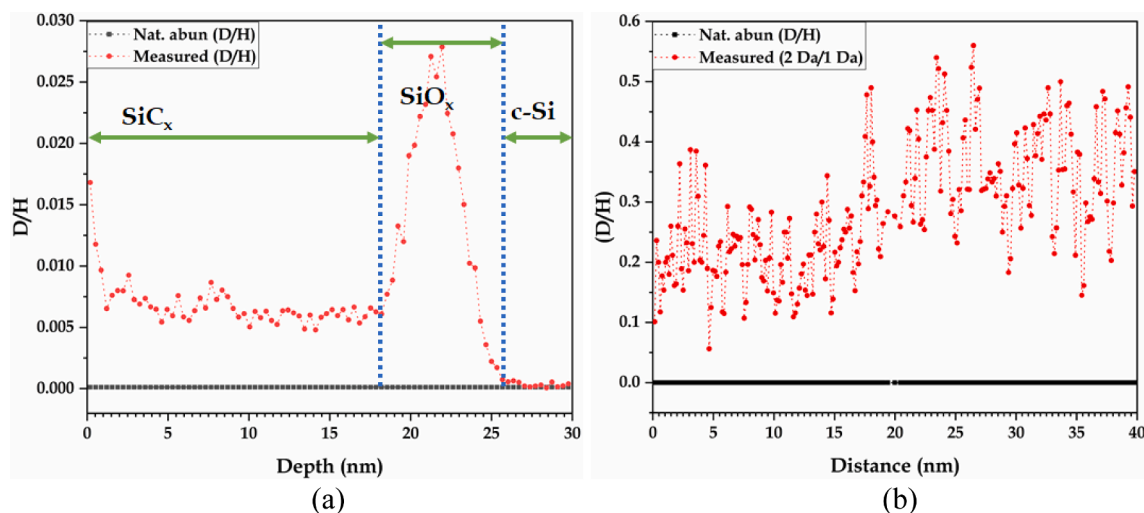
Fig. 8. Measured 2 Da/H ratio compared with natural abundance of D for (a) SIMS; (b) APT.

layer for the present experimental case. A nonlinear response function within the analysed structure for the present case is the prime reason that we cannot directly compare the SIMS D/H ratio at the SiC_x and SiO_x layer with the APT 2 Da/H ratio for the respective layer. Since the wafer has uniform matrix concentration (single phase crystalline Si), here the response function should behave similarly as in a perfect experiment and SIMS intensity ratio for D/H should be directly comparable. There are already published reports regarding this type of broadening of the impurity profiles and depth resolution [53,54,56,58]. As in our current experiments, the matrix response function continuously changes from the SiC_x and SiO_x layer; therefore, the peak broadening effect may provide a plausible explanation for the absence of B, C peaks (cf. SI. Fig. S3) within the oxide layer in SIMS profile. The difference between the normalized O signal in the SiC_x and SiO_x layer for SIMS is low compared to the APT signal, suggesting a significant reduction in O peak intensity due to profile broadening caused by ion-beam mixing. Moreover, mass transport due to ion-beam mixing also causes a shift in the peaks for O, Si (cusp), H, and D towards the surface compared to APT profiles (see SI. Fig. 3S) along with blurring of the peak. Moreover, the relative shift in peak position in between H and D in SIMS profile could also be explained based on their diffusivity, in the light of mass-transport via ion beam mixing [56,59]. However, a detailed analysis of this topic is not in the scope of the current paper.

Fig. 9. Schematic showing the increase in adsorbed hydrogen during field evaporation.

3.2. Effect of adsorbed H_2 on APT analysis

Hydrogen coming from the chamber is adsorbed at the tip apex and continuously field evaporated as H^+ and H_2^+ ions during an APT experiment, contributing as a background in the H and D signal of an APT mass-spectra. That makes it difficult to quantify hydrogen or deuterium concentration within a hydrogenated sample, as the background signal is overlapped with real H and D signals. The mass difference (Δm) between H_2^+ and D^+ is ≈ 0.00154829, which requires a mass resolution, $m/\Delta m$, of ≈ 1300 to separate them in any mass-spectrometry experiment. The the atom probe (LEAP) instrument employed here has mass resolution up to 1000 which cannot differentiate between H_2^+ and D^+ [60]. Hence, even though APT acquisition takes place at ultra-high vacuum, it is common to have significant H^+ and H_2^+ contributions in H and D analysis using APT originate from H_2 molecule present in the analysis chamber. Prior to quantifying H and D using APT, an in-depth understanding of the formation of H^+ and H_2^+ signals from the chamber gas during field evaporation process is essential. Previous reports have demonstrated how experimental parameters affect the detected residual chamber gas (H^+ and H_2^+) during APT experiments [18,32,42,61,62]. Sundell et al. showed the effect of residual hydrogen during hydrogen detection in APT using laser pulsing and proposed the optimal parameters to reduce the contribution from adsorbed H_2 [27] significantly. They had reported an operating condition of 0.7nJ laser energy and 70°K sample temperature in order to detect residual gas contribution as low as ≈ 0.05 at.% in a crystalline Ni sample. Based on their report, we have also selected our experimental conditions to achieve a low background contribution. It was reported that at low temperature and ultra-high vacuum, field-evaporation of Si behaves similarly to metal surfaces [63]. Fig. 7 shows APT line profile of 1 Da, 2 Da, and their ratio throughout the whole reconstructed tip, including the Cr capping layer. The 1 Da and 2 Da profiles continuously rise until the Si-wafer side with a peak at the SiO_x layer. The absolute value of the 2 Da profile is much lower than the 1 Da profile. 1 Da signal also shows a peak even at the unwanted native oxide layer (see Fig. 2) formed between the Cr-capping and SiC_x layers. However, the 2 Da profile does not exhibit any peak at the unwanted native oxide layer, as seen in Fig. 7. One of the characteristics of the APT-line profile is a continuous increase in both the 1 Da and 2 Da signal even at the Si-wafer side, which is different from the observed trend in the SIMS experiment, see Fig. 4. Secondly, it is necessary to differentiate whether the 2 Da peak at the SiO_x layer stems from the trapping of D within that layer like H or the production of a higher amount of H_2^+ ions coming from a higher H concentration at that layer. In order to approach these issues, let's first discuss the formation mechanism of H^+ and H_2^+ ions from the chamber
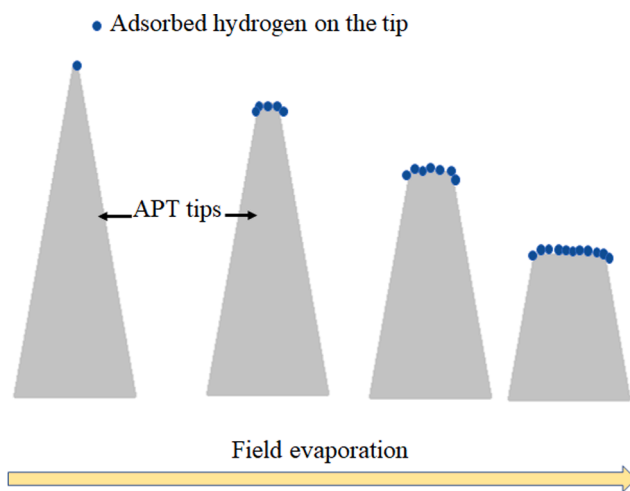
Table 1

Ratio of integrated intensity of peaks corresponding to both doubly and single charged Si isotopes. Mass spectra were constructed by selecting signal from the whole tip, as well as from only the Si-wafer side. Doubly charged Si is consistent with the natural abundance ratio of Si. However, singly charged Si does not obey the natural abundance ratio due to interference from the formation of complex molecular ions, such as $^{28}Si^1H^+$, $^{28}Si^2D^+$.

Portion of the sample	Element and charge state	Mass 28	Mass 29	Mass 30
	Si natural abundance	92.2	4.7	3.1
Whole tip	Si^{++}	91.7	5	3.3
	Si$^+$	64.1	23.8	12.1
c-Si-wafer side	Si^{++}	92.4	4.6	3.0
	Si$^+$	76.1	22.2	1.7

gas during field evaporation in a pulsed laser APT experiment, contributing as a background signal. Hydrogen from the analysis chamber adsorbs onto the tip surface due to the presence of a high electric field and is subsequently desorbed during field evaporation [64]. Therefore, continuous desorption of the adsorbed H requires a steady supply of the H_2 molecules at the high field area of the tip apex from the available chamber gas. It was reported that the main supply mechanism of H at the tip apex is adsorption of the H adatoms at the protruding tip apex through field assisted dipole-image dipole interaction [27] or surface diffusion of the H atoms via the shank [65]. Field evaporation of the APT tip makes the tip blunt and increases the tip apex area; therefore, to maintain a constant field for evaporation viz evaporation rate, a high energy laser pulse is combined with an increasing DC voltage applied on the tip for a typical pulsed laser APT experiment. An increase in the tip apex area increases the total surface area coverage at the tip apex for H adatoms through enhancement in field-assisted adsorption by the increase in DC voltage [27]. This process is depicted with the help of a simple schematic in Fig. 9. As a result, both the 1 Da and 2 Da line profiles show a continuous increase in the signal at the wafer side. Sundell et al., in their experiment, showed that at 0.3 nJ laser power initially with increasing the DC voltage the intensity of both H$^+$ and H$_2^+$ increases and after reaching a certain DC voltage, adsorption drops off, and H$_2^+$ intensity starts to decrease slowly [27]. Although both the analysed material and experimental parameters are different in the present case, the trend in the H$^+$ and H$_2^+$ is quite similar, especially at the Si-wafer side, as seen in Fig. 7. The DC voltage reaches up to a maximum value of ≈5500 V for our experiment, see SI. Fig. S5, much lower than

Sundell et al. experiment. That may indicate why we have not observed a decrease in both H$^+$ and H$_2^+$ concentration at the wafer side, as shown in Fig. 7.

A closer inspection of the APT mass spectra further helps in distinguishing between the trapped H and D within the layers from the background contribution of adsorbed H$_2$ originated from chamber gas. Table 1 displays the ratio of the integrated intensity of single and doubly charged Si isotopes peaks, calculated from the mass-spectra, obtained from the whole tip as well as only from the Si-wafer. Doubly charged Si peaks in the mass spectra follow isotopic abundance, whether from the whole tip or only from the Si-wafer. Even the absolute intensity counts of doubly charged Si is much higher than the single charged Si as seen in SI. Fig. S1. APT mass-spectra of the whole tip shows three distinct peaks at 28, 29, and 30 Da, corresponding to single charged three natural isotopes of Si. During the laser pulsed APT experiment, it is known that complex molecular ions are detected in the mass spectra. Therefore, the peak at 29 and 30 Da in the mass-spectra should not only be assigned to single charged ^{29}Si and ^{30}Si, but it is also overlapped with ($^{28}Si^1H$)$^+$, ($^{28}Si^2D$)$^+$, and ($^{28}Si^1H_2$)$^+$. Here, we purposefully neglect the complex molecular ions formed with ^{29}Si and ^{30}Si as their fractions are already low in the natural abundance of Si. The integrated intensity ratio of peaks at 28, 29, and 30 Da further supports our complex ion formation argument. They do not follow the natural abundance of Si, unlike the doubly charged species of Si, as seen in Table 1. Furthermore, on the wafer side, the fraction of 29 and 30 Da seen in Table 1 is very different from the values corresponding to the natural abundances of ^{29}Si and ^{30}Si. While the fraction of mass 29 is much higher than the natural abundance of ^{29}Si, there is a lower fraction of both mass 28 and 30 when compared to the natural abundances of ^{28}Si and ^{30}Si, respectively. Therefore, it can be concluded that ($^{28}Si^1H$)$^+$ is the main complex ion that is produced and that the contribution from ($^{28}Si^1H_2$)$^+$ is negligible during the pulsed laser field evaporation of the Si-wafer. 1D line profiles of mass 29, 30, and 1, 2 Da, shown in SI. Fig. S6a and b, further strengthen our argument. The 1 and 2 Da signals (see SI. Fig. 6b) both display a peak at the SiO$_x$ layer followed by a rising signal at Si-wafer. On the other hand, the 1D-line profile of mass 29 and 30 (see SI. Fig. 6a) shows a peak at the SiO$_x$ layer (SiC$_x$/SiO$_x$ interface) and a stable low signal in the Si-wafer. On the contrary, Si signal shows a dip in the SiO$_x$ layer as the concentration of Si is lower within the layer. Therefore, the mass 29 and 30 signals in the oxide layer are mostly associated with the complex ion formation, namely ($^{28}Si^1H$)$^+$ and ($^{28}Si^2D$)$^+$ respectively during field evaporation. The contribution of monoatomic $^{29}Si^+$ and
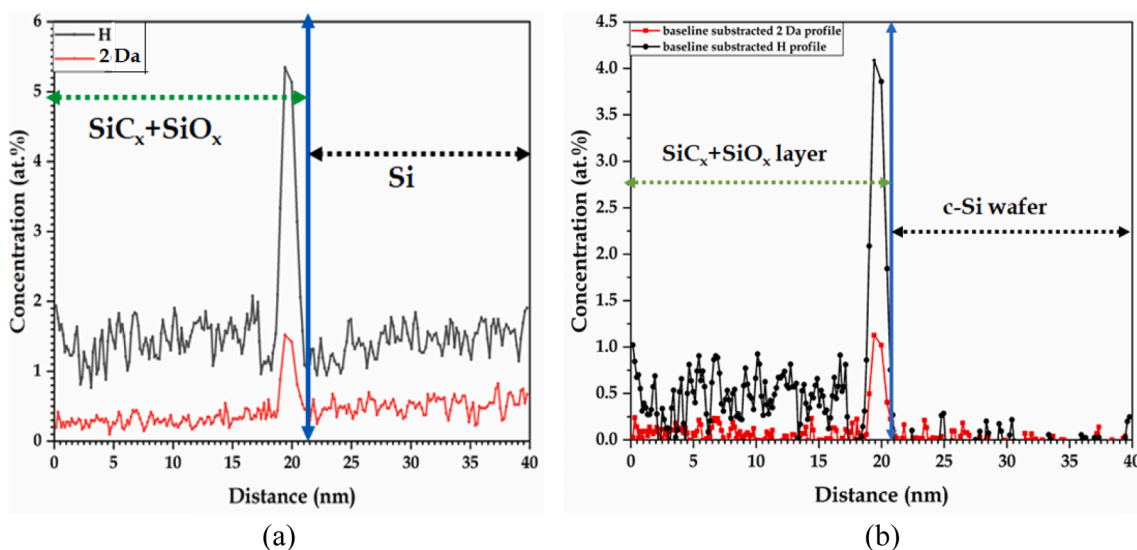
Fig. 10. Measured 1D-APT profile showing compositional variation of 1 Da and 2 Da across different layers, (a) without background correction; (b) after background correction.
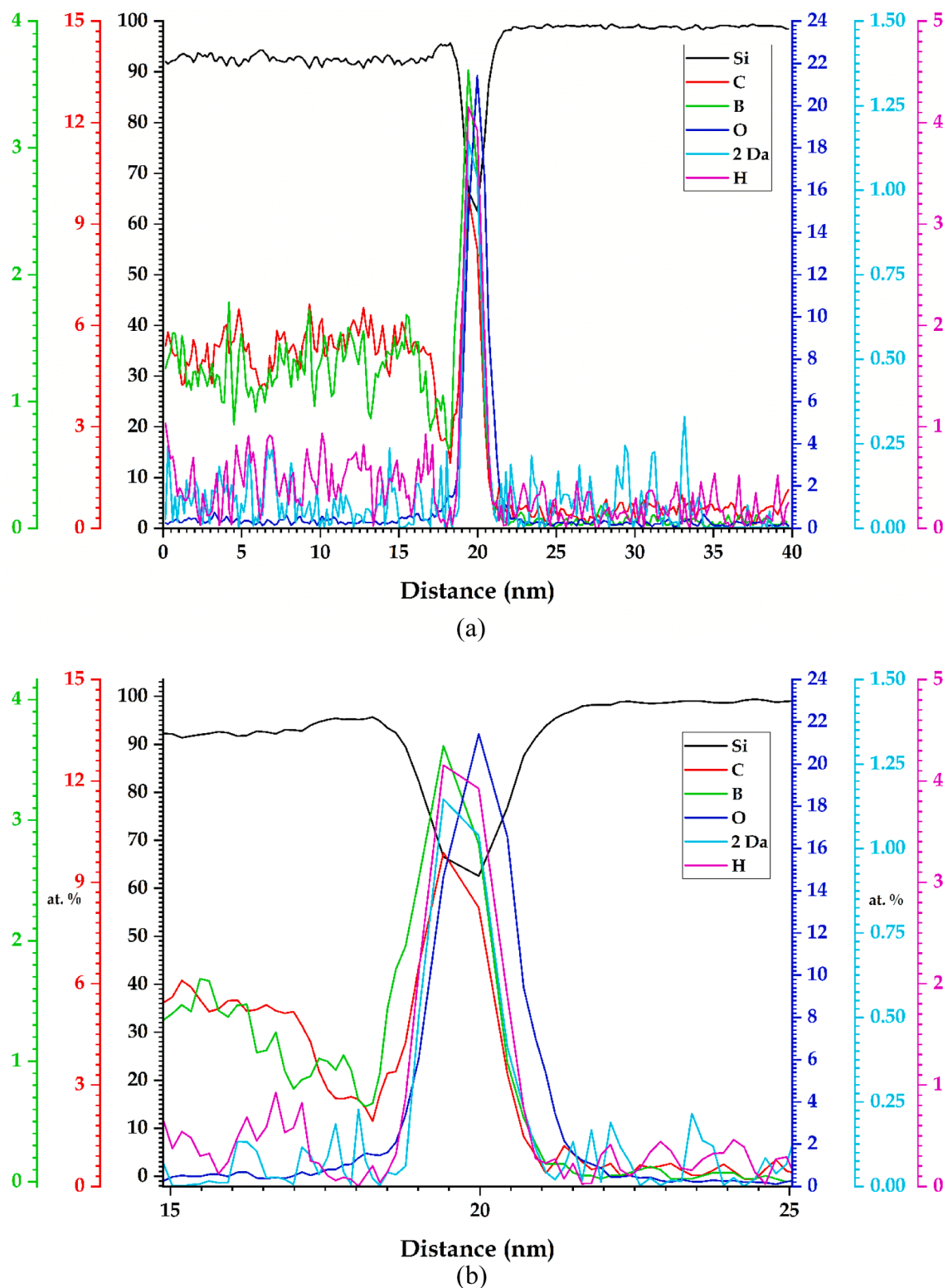
Fig. 11. (a) Modified APT composition profile after background subtraction from 1 Da (H) and 2 Da profile, (b) A magnified view centred on the oxide layer.

$^{30}Si^+$ on the line profile of 29 and 30 Da is negligible because the fraction of $^{29}Si^+$ and ^{30}Si in the natural abundance of Si is ≈ 4.7 and 3.1%, respectively. The tendency of complex molecular ion $(^{28}Si^1H)^+$, $(^{28}Si^2D)^+$ formation increases only from those regions, where both H and D is trapped with higher binding energy. The binding energy of adsorbed hydrogen with Si is a few tenths of an electron-volt [63]. The probability of formation of complex molecular ions like SiH_2^+ over SiH^+ and SiD^+ is

lower for the current experimental conditions, as the tip voltage is not significantly high but the laser power and pulse frequency is high [63].

Based on the SIMS data, we can conclusively comment that both H and D are trapped at the SiO_x layer through higher binding energy. Notably, at the unwanted native oxide layer between the Cr-capping and SiC_x layer, H concentration is also high, which is expected from the PVD deposition of the Cr-capping layer. However, no significant increase in

the 2 Da (H_2^+) concentration was observed at the same region, suggesting that an increase in the adsorbed H^+ content does not necessarily increase the H_2^+ content during pulsed laser field evaporation. Therefore, the peak in the 2 Da profile at the SiO_x layer is not related to H_2^+ stemming from more H in the layer; instead, it is associated with D's trapping within that layer which is consistent with the SIMS analysis.

3.3. Background correction of APT composition profile using SIMS

The preceding section illustrated how hydrogen adsorbed on the tip surface and field evaporation contribute as a background in the APT concentration profile analysis. Notably, this adsorbed hydrogen from the analysis chamber also affects the D composition profile obtained from the APT analysis by producing an H_2^+ ionized state. SIMS results provide reliable isotopic measurements thanks to its mass resolution and sensitivity. Therefore, the SIMS profile can be used to deconvolute the background contribution from the D profile obtained in the APT analysis. In Fig. 8a, the D/H ratio measured from SIMS is plotted for comparison with the natural isotopic ratio. Fig. 8a shows that within the Si wafer, the measured D/H ratio from SIMS drops to its natural abundance. Moreover, D enrichment is clearly seen in the layer of SiC_x followed by a peak at the SiO_x layer. Notably, the peak in the measured D/H ratio is associated with the oxide layer. On the other hand, the measured 2 Da/H ratio from APT, see Fig. 8b, does not drop to its natural abundance in the substrate side, instead, it shows a continuously increasing trend due to background contribution from the residual chamber gas. Hence, a conservative approach was taken to correct the APT D profile based on the insights from the SIMS D profile (see Fig. 4). A baseline has been created using the spline interpolated method [66], which is further extrapolated to the SiC_x layer. The boundary condition for the baseline is determined from the SIMS D/H ratio, that even in the APT dataset the 2 Da/H ratio should also reach the value 0.000115 (natural isotopic ratio of D/H). At the start of pulsed laser APT experiment the background contribution of H^+ and H_2^+ will be low near the tip due to a low applied voltage at the tip [63]. We further extend our approach to the hydrogen analysis. As both H and D have a similar chemical affinity, both show a peak at the SiO_x layer and enrichment in the SiC_x layer. D-SIMS profile analysis certainly confirms the trapping of both H and D in the SiC_x and SiO_x layer, while the SiO_x layer emerges as the strongest trapping sites with a peak in D-SIMS intensity at the oxide layer. The H signal detected in the wafer for both APT and SIMS is only due to the residual chamber gas since SIMS profiling does not find excess D in the wafer above its natural abundance. Hence, similar to the D-APT composition profile, background contribution has also been subtracted from the H-APT profile extrapolating the background profile of the Si-wafer side. For comparison, uncorrected profiles for H and mass 2 Da are also shown in Fig. 10a. After background subtraction, the modified APT 1D-composition profile is also shown in Fig. 10b. Background corrected and modified composition profiles for all the elements are shown in Fig. 11. The oxide layer's average composition after background subtraction is Si- 59.1, C-9.9, B-3.9, O-21.6, D- 1.2, and H-4.3 at. %, respectively. As a side note, APT measured O/Si ratio within the oxide layer by integrating the area under the APT composition profile is ≈ 0.30, whereas the O/Si ratio within the oxide layer measured from EDS is ≈ 0.34, following the similar method. This discrepancy could be attributed to the fact that EDS is volume averaged, including possible surface oxidation, and that it is not a UHV analysis, unlike APT.

4. Conclusions

The present study introduces a new correlative method combining TEM, SIMS, and APT to address the analytical challenges in detecting and quantifying hydrogen in nanoscale layers. The hydrogen concentration in a hydrogenated contact containing c-Si/SiO_x/nc-SiC_x(p) stack was investigated. Both the hydrogen and deuterium diffuse through the SiC_x layer and get trapped within the thin SiO_x layer after hydrogenation. Thermal annealing produces C and B rich nanoclusters within the SiC_x layer and a significant amount of hydrogen and deuterium are also trapped within the SiC_x layer. Both C and B diffuses into the SiO_x layer. Hydrogen and deuterium peaks within the oxide layer are closer to the SiC_x/SiO_x interface. The APT analysis shows the oxide layer is non-stoichiometric. SIMS successfully detects both hydrogen and deuterium's presence within the layer. SIMS depth profiling shows deuterium to hydrogen ratio in the Si side reaches its natural abundance; whereas, the APT line profile suffers from background contribution from the residual chamber gas and displays a high hydrogen and 2 Da concentration within the Si-wafer side of the stack. The background contribution has been successfully deconvoluted from the real hydrogen and deuterium concentration profile within the stack in APT data by modelling the background using a spline interpolation method, where the deuterium to hydrogen ratio within the Si side, measured using SIMS, serves as a guiding tool for baseline determination. The current methodology offers a reduction in the number of experiments needed to be performed separately in both SIMS and APT for near accurate measurement of hydrogen in a nanometer-scale structure. More precisely, controlled experiments on standard samples for accurate quantification could possibly be avoided by adopting the proposed methodology. The hydrogen content is about 1 at.% within the SiC_x layer and 4.3 at.% within the SiO_x layer. The present correlative study paves the way for a comprehensive quantitative understanding of the role of hydrogen in nanoscale structures and its influence in determining the macroscale device properties.

Declaration of Competing Interest

The authors declare that they have no known competing financial interests or personal relationships that could have appeared to influence the work reported in this paper.

Appendix A. Supplementary material

Supplementary data to this article can be found online at https://doi.org/10.1016/j.apsusc.2021.149650.

References:

[1] ISE, Photovoltaics Report Fraunhofer Institute for Solar Energy Systems, 2012.
[2] N.R.E.L. (NREL), Best Research Efficiency, Http://Www.Nrel.Gov/Ncpv/Images/Efficiency_Chart.Jpg. (2016). http://www.nrel.gov/ncpv/images/efficiency_chart.jpg.
[3] A. Cuevas, Physical model of back line-contact front-junction solar cells, J. Appl. Phys. 113 (2013), 164502, https://doi.org/10.1063/1.4800840.
[4] A. Metz, D. Adler, S. Bagus, H. Blanke, M. Bothar, E. Brouwer, S. Dauwe, K. Dressler, R. Droessler, T. Droste, M. Fiedler, Y. Gassenbauer, T. Grahl, N. Hermert, W. Kuzminski, A. Lachowicz, T. Lauinger, N. Lenck, M. Manole, M. Martini, R. Messmer, C. Meyer, J. Moschner, K. Ramspeck, P. Roth, R. Schönfelder, B. Schum, J. Sticksel, K. Vaas, M. Volk, K. Wangemann, Industrial high performance crystalline silicon solar cells and modules based on rear surface passivation technology, Sol. Energy Mater. Sol. Cells 120 (2014) 417–425, https://doi.org/10.1016/j.solmat.2013.06.025.
[5] A. Richter, J. Benick, F. Feldmann, A. Fell, M. Hermle, S.W. Glunz, n-Type Si solar cells with passivating electron contact: identifying sources for efficiency limitations by wafer thickness and resistivity variation, Sol. Energy Mater. Sol. Cells 173 (2017) 96–105, https://doi.org/10.1016/j.solmat.2017.05.042.
[6] F. Haase, C. Hollemann, S. Schäfer, A. Merkle, M. Rienäcker, J. Krügener, R. Brendel, R. Peibst, Laser contact openings for local poly-Si-metal contacts enabling 26.1%-efficient POLO-IBC solar cells, Sol. Energy Mater. Sol. Cells 186 (2018) 184–193.

[7] E. Bellini, JinkoSolar claims 24.9% efficiency for n-type monocrystalline cell, (n. d.). https://www.pv-magazine.com/2021/01/06/jinkosolar-claims-24-9-efficiency-for-n-type-monocrystalline-cell/.

[8] A. Richter, 26% Efficiency with Both Sides Contacted Silicon Solar Cells: Front vs Rear Junction Cell Architecture, in: SiliconPV 2020, 2020. https://video2020.siliconpv.com/upload-video/list.

[9] S. Duttagupta, N. Nandakumar, P. Padhamnath, J.K. Buatis, R. Stangl, A.G. Aberle, monoPoly^{TM} cells: large-area crystalline silicon solar cells with fire-through screen printed contact to doped polysilicon surfaces, Sol. Energy Mater. Sol. Cells. 187 (2018) 76–81, https://doi.org/10.1016/j.solmat.2018.05.059.

[10] F. Ye, W. Deng, W. Guo, R. Liu, D. Chen, Y. Chen, Y. Yang, N. Yuan, J. Ding, Z. Feng, P.P. Altermatt, P.J. Verlinden, 22.13% Efficient industrial p-type mono PERC solar cell, in: 2016 IEEE 43rd Photovolt. Spec. Conf., 2016: pp. 3360–3365. https://doi.org/10.1109/PVSC.2016.7750289.

[11] G. Dingemans, W. Beyer, M.C.M. van de Sanden, W.M.M. Kessels, Hydrogen induced passivation of Si interfaces by Al2O3 films and SiO2/Al2O3 stacks, Appl. Phys. Lett. 97 (2010) 152106, https://doi.org/10.1063/1.3497014.

[12] N.M. Johnson, D.K. Biegelsen, M.D. Moyer, Low-temperature annealing and hydrogenation of defects at the Si–SiO2 interface, J. Vac. Sci. Technol. 19 (1981) 390–394, https://doi.org/10.1116/1.571070.

[13] M. Schnabel, B.W.H. van de Loo, W. Nemeth, B. Macco, P. Stradins, W.M. M. Kessels, D.L. Young, Hydrogen passivation of poly-Si/SiOx contacts for Si solar cells using Al2O3 studied with deuterium, Appl. Phys. Lett. 112 (2018), 203901, https://doi.org/10.1063/1.5031118.

[14] M. Lehmann, N. Valle, J. Horzel, A. Pshenova, P. Wyss, M. Döbeli, M. Despeisse, S. Eswara, T. Wirtz, Q. Jeangros, A. Hessler-Wyser, F.J. Haug, A. Ingenito, C. Ballif, Analysis of hydrogen distribution and migration in fired passivating contacts (FPC), Sol. Energy Mater. Sol. Cells. 200 (2019), 110018, https://doi.org/10.1016/j.solmat.2019.110018.

[15] F.G. Wei, K. Tsuzaki, Quantitative analysis on hydrogen trapping of TiC particles in steel, Metall. Mater. Trans. A. 37 (2006) 331–353, https://doi.org/10.1007/s11661-006-0004-3.

[16] P.C. Zalm, Dynamic SIMS: Quantification at all depths? Mikrochim. Acta. 132 (2000) 243–257, https://doi.org/10.1007/s006040050018.

[17] J.C. Meyer, C.O. Girit, M.F. Crommie, A. Zettl, Imaging and dynamics of light atoms and molecules on graphene, Nature 454 (2008) 319–322, https://doi.org/10.1038/nature07094.

[18] G. Sundell, M. Thuvander, A.K. Yatim, H. Nordin, H.O. Andrén, Direct observation of hydrogen and deuterium in oxide grain boundaries in corroded Zirconium alloys, Corros. Sci. 90 (2015) 1–4, https://doi.org/10.1016/j.corsci.2014.10.016.

[19] J. Takahashi, K. Kawakami, Y. Kobayashi, T. Tarui, The first direct observation of hydrogen trapping sites in TiC precipitation-hardening steel through atom probe tomography, Scr. Mater. 63 (2010) 261–264, https://doi.org/10.1016/j.scriptamat.2010.03.012.

[20] J. Takahashi, K. Kawakami, T. Tarui, Direct observation of hydrogen-trapping sites in vanadium carbide precipitation steel by atom probe tomography, Scr. Mater. 67 (2012) 213–216, https://doi.org/10.1016/j.scriptamat.2012.04.022.

[21] Y.-S. Chen, D. Haley, S.S.A. Gerstl, A.J. London, F. Sweeney, R.A. Wepf, W.M. Rainforth, P.A.J. Bagot, M.P. Moody, Direct observation of individual hydrogen atoms at trapping sites in a ferritic steel, Science (80-.). 355 (2017) 1196 LP–1199. https://doi.org/10.1126/science.aal2418.

[22] Y.-S. Chen, H. Lu, J. Liang, A. Rosenthal, H. Liu, G. Sneddon, I. McCarroll, Z. Zhao, W. Li, A. Guo, J.M. Cairney, Observation of hydrogen trapping at dislocations, grain boundaries, and precipitates, Science (80-.) 367 (2020) 171 LP–175. https://doi.org/10.1126/science.aaz0122.

[23] K. Inoue, F. Yano, A. Nishida, H. Takamizawa, T. Tsunomura, Y. Nagai, M. Hasegawa, Dopant distributions in n-MOSFET structure observed by atom probe tomography, Ultramicroscopy 109 (2009) 1479–1484, https://doi.org/10.1016/j.ultramic.2009.08.002.

[24] H. Takamizawa, Y. Shimizu, K. Inoue, T. Toyama, N. Okada, M. Kato, H. Uchida, F. Yano, A. Nishida, T. Mogami, Y. Nagai, Origin of characteristic variability in metal-oxide-semiconductor field-effect transistors revealed by three-dimensional atom imaging, Appl. Phys. Lett. 99 (2011), 133502, https://doi.org/10.1063/1.3644960.

[25] B. Han, H. Takamizawa, Y. Shimizu, K. Inoue, Y. Nagai, F. Yano, Y. Kunimune, M. Inoue, A. Nishida, Phosphorus and boron diffusion paths in polycrystalline silicon gate of a trench-type three-dimensional metal-oxide-semiconductor field effect transistor investigated by atom probe tomography, Appl. Phys. Lett. 107 (2015) 23506, https://doi.org/10.1063/1.4926970.

[26] Y. Kunimune, Y. Shimada, Y. Sakurai, M. Inoue, A. Nishida, B. Han, Y. Tu, H. Takamizawa, Y. Shimizu, K. Inoue, F. Yano, Y. Nagai, T. Katayama, T. Ide, Quantitative analysis of hydrogen in SiO2/SiN/SiO2 stacks using atom probe tomography, AIP Adv. 6 (2016) 45121, https://doi.org/10.1063/1.4948558.

[27] G. Sundell, M. Thuvander, H.-O. Andrén, Hydrogen analysis in APT: Methods to control adsorption and dissociation of H2, Ultramicroscopy. 132 (2013) 285–289, https://doi.org/10.1016/j.ultramic.2013.01.007.

[28] B.P. Gorman, A.G. Norman, Y. Yan, Atom probe analysis of III–V and Si-based semiconductor photovoltaic structures, Microsc. Microanal. 13 (2007) 493–502, https://doi.org/10.1017/S1431927607070894.

[29] G. McMahon, B.D. Miller, M.G. Burke, High resolution NanoSIMS imaging of deuterium distributions in 316 stainless steel specimens after fatigue testing in high pressure deuterium environment, Npj Mater. Degrad. 2 (2018) 1–6, https://doi.org/10.1038/s41529-017-0023-0.

[30] A. Röhsler, O. Sobol, H. Hänninen, T. Böllinghaus, In-situ ToF-SIMS analyses of deuterium re-distribution in austenitic steel AISI 304L under mechanical load, Sci. Rep. 10 (2020) 3611, https://doi.org/10.1038/s41598-020-60370-2.

[31] A. Röhsler, O. Sobol, W.E.S. Unger, T. Böllinghaus, Comprehensive study of deuterium-induced effects in austenitic stainless steel AISI 304L, Int. J. Hydrogen Energy 44 (2019) 12228–12238, https://doi.org/10.1016/j.ijhydene.2019.03.058.

[32] H. Takamizawa, K. Hoshi, Y. Shimizu, F. Yano, K. Inoue, S. Nagata, T. Shikama, Y. Nagai, Three-dimensional characterization of deuterium implanted in silicon using atom probe tomography, Appl. Phys. Express. 6 (2013), https://doi.org/10.7567/APEX.6.066602.

[33] V.R. Deline, W. Katz, C.A. Evans, P. Williams, Mechanism of the SIMS matrix effect, Appl. Phys. Lett. 33 (1978) 832–835, https://doi.org/10.1063/1.90546.

[34] A. Franquet, B. Douhard, D. Melkonyan, P. Favia, T. Conard, W. Vandervorst, Self Focusing SIMS: Probing thin film composition in very confined volumes, Appl. Surf. Sci. 365 (2016) 143–152, https://doi.org/10.1016/j.apsusc.2016.01.056.

[35] K. Li, T. Aarholt, J. Liu, H. Hulme, A. Garner, M. Preuss, S. Lozano-Perez, C. Grovenor, 3D-characterization of deuterium distributions in zirconium oxide scale using high-resolution SIMS, Appl. Surf. Sci. 464 (2019) 311–320, https://doi.org/10.1016/j.apsusc.2018.09.101.

[36] J. Hu, T. Aarholt, B. Setiadinata, K. Li, A. Garner, S. Lozano-Perez, M. Moody, P. Frankel, M. Preuss, C. Grovenor, A multi-technique study of "barrier layer" nano-porosity in Zr oxides during corrosion and hydrogen pickup using (S)TEM, TKD, APT and NanoSIMS, Corros. Sci. 158 (2019) 108109, https://doi.org/10.1016/j.corsci.2019.108109.

[37] G. Da Rosa, P. Maugis, A. Portavoce, J. Drillet, N. Valle, E. Lentzen, K. Hoummada, Grain-boundary segregation of boron in high-strength steel studied by nano-SIMS and atom probe tomography, Acta Mater. 182 (2020) 226–234, https://doi.org/10.1016/j.actamat.2019.10.029.

[38] A. Ingenito, G. Nogay, Q. Jeangros, E. Rucavado, C. Allebé, S. Eswara, N. Valle, T. Wirtz, J. Horzel, T. Koida, M. Morales-Masis, M. Despeisse, F.-J. Haug, P. Löper, C. Ballif, A passivating contact for silicon solar cells formed during a single firing thermal annealing, Nat. Energy. 3 (2018) 800–808, https://doi.org/10.1038/s41560-018-0239-4.

[39] Y. Kunimune, Y. Shimada, Y. Sakurai, M. Inoue, A. Nishida, B. Han, Y. Tu, H. Takamizawa, Y. Shimizu, K. Inoue, F. Yano, Y. Nagai, T. Katayama, T. Ide, Quantitative analysis of hydrogen in SiO2/SiN/SiO2 stacks using atom probe tomography, AIP Adv. 6 (2016) 10–17, https://doi.org/10.1063/1.4948558.

[40] F.A. Stevie, C. Zhou, M. Hopstaken, M. Saccomanno, Z. Zhang, A. Turansky, SIMS measurement of hydrogen and deuterium detection limits in silicon: Comparison of different SIMS instrumentation, J. Vac. Sci. Technol. B, Nanotechnol. Microelectron. Mater. Process. Meas. Phenom. 34 (2016) 03H103, https://doi.org/10.1116/1.4940151.

[41] B.W.H. Van De Loo, B. Macco, M. Schnabel, M.K. Stodolny, A.A. Mewe, D.L. Young, W. Nemeth, P. Stradins, W.M.M. Kessels, Solar energy materials and solar cells on the hydrogenation of Poly-Si passivating contacts by Al 2 O 3 and SiN x thin films, Sol. Energy Mater. Sol. Cells. 215 (2020), 110592, https://doi.org/10.1016/j.solmat.2020.110592.

[42] I. Mouton, A.J. Breen, S. Wang, Y. Chang, A. Szczepaniak, P. Kontis, L. T. Stephenson, D. Raabe, M. Herbig, T. Ben Britton, B. Gault, Quantification challenges for atom probe tomography of hydrogen and deuterium in zircaloy-4, Microsc. Microanal. Off. J. Microsc. Soc. Am. Microbeam Anal. Soc. Microsc. Soc. Canada. 25 (2019) 481–488, https://doi.org/10.1017/S143192761801615X.

[43] D. Tweddle, P. Hamer, Z. Shen, V.P. Markevich, M.P. Moody, P.R. Wilshaw, Direct observation of hydrogen at defects in multicrystalline silicon, Prog. Photovoltaics Res. Appl. (2019) https://doi.org/https://doi.org/10.1002/pip.3184.

[44] A. Moldovan, F. Feldmann, G. Krugel, M. Zimmer, J. Rentsch, M. Hermle, A. Roth-Fölsch, K. Kaufmann, C. Hagendorf, Simple cleaning and conditioning of silicon surfaces with UV/ozone sources, Energy Proc. 55 (2014) 834–844, https://doi.org/10.1016/j.egypro.2014.08.067.

[45] A. Fukano, H. Oyanagi, Highly insulating ultrathin SiO2 film grown by photooxidation, J. Appl. Phys. 94 (2003) 3345–3349, https://doi.org/10.1063/1.1597940.

[46] A. Moldovan, F. Feldmann, M. Zimmer, J. Rentsch, J. Benick, M. Hermle, Tunnel oxide passivated carrier-selective contacts based on ultra-thin SiO2 layers, Sol. Energy Mater. Sol. Cells. 142 (2015) 123–127, https://doi.org/https://doi.org/10.1016/j.solmat.2015.06.048.

[47] G. Nogay, J. Stuckelberger, P. Wyss, E. Rucavado, C. Allebé, T. Koida, M. Morales-Masis, M. Despeisse, F.-J. Haug, P. Löper, C. Ballif, Interplay of annealing temperature and doping in hole selective rear contacts based on silicon-rich silicon-carbide thin films, Sol. Energy Mater. Sol. Cells. 173 (2017) 18–24, https://doi.org/10.1016/j.solmat.2017.06.039.

[48] C.E. Blat, E.H. Nicollian, E.H. Poindexter, Mechanism of negative-bias-temperature instability, J. Appl. Phys. 69 (1991) 1712–1720, https://doi.org/10.1063/1.347217.

[49] K. Thompson, D. Lawrence, D.J. Larson, J.D. Olson, T.F. Kelly, B. Gorman, In situ site-specific specimen preparation for atom probe tomography, Ultramicroscopy. 107 (2007) 131–139, https://doi.org/10.1016/j.ultramic.2006.06.008.

[50] B. Stegemann, K.M. Gad, P. Balamou, D. Sixtensson, D. Vössing, M. Kasemann, H. Angermann, Ultra-thin silicon oxide layers on crystalline silicon wafers: comparison of advanced oxidation techniques with respect to chemically abrupt SiO 2/Si interfaces with low defect densities, Appl. Surf. Sci. 395 (2017) 78–85, https://doi.org/10.1016/j.apsusc.2016.06.090.

[51] K. Wittmaack, Background formation in SIMS analysis of hydrogen, carbon, nitrogen and oxygen in silicon, Nucl. Instruments Methods Phys. Res. 218 (1983) 327–332, https://doi.org/10.1016/0167-5087(83)91001-3.

[52] C.W. Magee, E.M. Botnick, Hydrogen depth profiling using sims - problems and their solutions, J. Vac. Sci. Technol. 19 (1981) 47–52, https://doi.org/10.1116/1.571015.

[53] P.P. Michałowski, W. Kaszub, A. Merkulov, W. Strupiński, Secondary ion mass spectroscopy depth profiling of hydrogen-intercalated graphene on SiC, Appl. Phys. Lett. 109 (2016), https://doi.org/10.1063/1.4958144.

[54] M. Cwil, P. Konarski, J. Ciosek, Ion mass interferences and matrix effects on SIMS depth profiling of thin Ti/Si multilayer films induced by hydrogen, carbon and oxygen contaminations, Int. J. Mass Spectrom. 263 (2007) 54–58, https://doi.org/10.1016/j.ijms.2006.12.004.

[55] K. Wittmaack, Transient phenomena and impurity relocation in SIMS depth profiling using oxygen bombardment: pursuing the physics to interpret the data, Philos. Trans. R. Soc. A Math. Phys. Eng. Sci. 354 (1996) 2731–2764, https://doi.org/10.1098/rsta.1996.0126.

[56] M. Saggio, C. Montandon, A. Bourenkov, L. Frey, P. Pichler, Distortion of sims profiles due to ion beam mixing, Radiat. Eff. Defects Solids. 141 (1997) 37–52, https://doi.org/10.1080/10420159708211555.

[57] M.G. Dowsett, R. Collins, M.G. Dowsett, E.H. Parker, M. Prutton, R.H. Williams, Noise, resolution and entropy in sputter profiling, Philos. Trans. R. Soc. London. Ser. A Math. Phys. Eng. Sci. 354 (1996) 2713–2729, https://doi.org/10.1098/rsta.1996.0125.

[58] A.R. Chanbasha, A.T.S. Wee, Ultralow-energy SIMS for shallow semiconductor depth profiling, Appl. Surf. Sci. 255 (2008) 1307–1310, https://doi.org/10.1016/j.apsusc.2008.05.030.

[59] R. Collins, J.J. Jimenez-Rodriguez, M. Wadsworth, R. Badheka, Reliability of the diffusion approximation for the ballistic relocation function in atomic mixing by ion beams, J. Appl. Phys. 64 (1988) 1120–1124, https://doi.org/10.1063/1.341871.

[60] T.F. Kelly, M.K. Miller, Invited review article: Atom probe tomography, Rev. Sci. Instrum. 78 (2007), https://doi.org/10.1063/1.2709758.

[61] Y.H. Chang, I. Mouton, L. Stephenson, M. Ashton, G.K. Zhang, A. Szczpaniak, W. J. Lu, D. Ponge, D. Raabe, B. Gault, Quantification of solute deuterium in titanium deuteride by atom probe tomography with both laser pulsing and high-voltage pulsing: influence of the surface electric field, New J. Phys. 21 (2019), https://doi.org/10.1088/1367-2630/ab1c3b.

[62] R. Gemma, T. Al-Kassab, R. Kirchheim, A. Pundt, Analysis of deuterium in V-Fe5at. % film by atom probe tomography (APT), J. Alloys Compd. 509 (2011) S872–S876, https://doi.org/10.1016/j.jallcom.2010.11.122.

[63] G.L. Kellogg, Field evaporation of silicon and field desorption of hydrogen from silicon surfaces, Phys. Rev. B 28 (1983) 1957–1964, https://doi.org/10.1103/PhysRevB.28.1957.

[64] D.F. Barofsky, E.W. Müller, Mass spectrometric analysis of low temperature field evaporation, Surf. Sci. 10 (1968) 177–196, https://doi.org/10.1016/0039-6028(68)90018-6.

[65] T.T. Tsong, E.W. Müller, Field adsorption of inert-gas atoms, J. Chem. Phys. 55 (1971) 2884–2889, https://doi.org/10.1063/1.1676510.

[66] S. Jahani, S.K. Setarehdan, D.A. Boas, M.A. Yücel, Motion artifact detection and correction in functional near-infrared spectroscopy: a new hybrid method based on spline interpolation method and Savitzky-Golay filtering, Neurophotonics. 5 (2018) 1–11, https://doi.org/10.1117/1.NPh.5.1.015003.